Astronomy & Astrophysics manuscript no. paper˙v4˙FinalVersion˙Submitted˙ArXiv
December 11, 2012
© ESO 2012

arXiv:1212.2151v1 [astro-ph.CO] 10 Dec 2012

AGN and QSOs in the eROSITA All-Sky Survey

Part I: Statistical properties

Alexander Kolodzig[1], Marat Gilfanov[1,2], Rashid Sunyaev[1,2], Sergey Sazonov[2], Marcella Brusa[3,4]

[1] Max-Planck-Institut für Astrophysik (MPA), Karl-Schwarzschild-Str. 1, D-85741 Garching, Germany, e-mail: alex@mpa-garching.mpg.de
[2] Space Research Institute (IKI), Russian Academy of Sciences, Profsoyuznaya ul. 84/32, Moscow, 117997 Russia
[3] Max-Planck-Institut für extraterrestrische Physik (MPE), Giessenbachstrasse, Postfach 1312, D-85741 Garching, Germany
[4] Dipartimento di Fisica e Astronomia, Universitá di Bologna, viale Berti Pichat 6/2, 40127 Bologna Italy

Received ? 2012; accepted ? 2012

ABSTRACT

Context. The main element of the observing program of the Spectrum-Roentgen-Gamma orbital observatory is a 4-years all-sky survey in the course of which the entire sky will be scanned eight times.
Aims. We analyze statistical properties of AGN and QSO to be detected in the course of the eROSITA all-sky survey (eRASS).
Methods. Given the currently planned survey strategy, parameters of the galactic and extragalactic X-ray background and results of the recent calculations of the eROSITA instrumental background, we compute the sensitivity map of the eRASS. Using the best available redshift-dependent AGN X-ray luminosity function (XLF) we compute various characteristics of the eRASS AGN sample, such as the luminosity and redshift distributions and the brightness distributions of their optical counterparts.
Results. After four years of the survey, the sky-average sensitivity of $\approx 10^{-14}$ erg s^{-1} cm^{-2} will be achieved in the $0.5-2.0$ keV band. With this sensitivity, eROSITA will detect about ≈ 3 million of AGN on the extragalactic sky ($|b| > 10°$). The median redshift of the eRASS AGN will be $z = 1$ with ≈ 40 % of objects in the $z = 1-2$ redshift range. There will be about $\sim 10^4 - 10^5$ AGN beyond redshift $z = 3$ and about $\sim 2\,000 - 30\,000$ AGN beyond redshift $z = 4$, the exact numbers depending on the poorly known behavior of the AGN XLF in the high redshift and luminosity regimes. The 10 % of brightest AGN will be detected with more than ≈ 38 counts per PSF HEW, whereas the 10 % of faintest objects will have less than ≈ 9 counts. The optical counterparts of about ~ 95 % of AGN will be brighter than $I_{\rm AB} = 22.5$ mag. The planned scanning strategy will allow one to search for transient events on the time scale of a half a year and a ∼few hours with the $0.5-2.0$ keV sensitivity of $\sim 2\times10^{-14} - \sim 2\times10^{-13}$ erg s^{-1} cm^{-2} respectively.

Key words. Surveys – X-rays: general – X-rays: galaxies – Quasars: general – Galaxies: active – Galaxies: luminosity function

1. Introduction

Large samples of X-ray detected active galactic nuclei (AGN), combined with follow up optical data for identification of objects and their redshift determination, are fundamental to understand AGN evolution and the growth of supermassive black holes (SMBHs) with cosmic time. These samples are constructed in various extragalactic X-ray surveys spanning from wide-shallow to narrow-deep surveys. Many of these have been performed in the last decade with Chandra and XMM-Newton X-ray observatories, which were instrumental in understanding the cosmic X-ray background and evolution of AGN at low and high redhifts (Brandt & Hasinger 2005). However, the last *all-sky survey* (Voges et al. 1999) in the X-ray band was performed by the ROSAT[1] (Truemper 1993) over two decades ago, creating an increasing demand for an all-sky survey to be conducted by the new generation of X-ray telescopes.

Table 1. Predicted background count rates.

Energy band [keV]	$0.5-2.0$	$2-10$
Particle	0.3	2.6
Galactic	1.8	0.0
Extragalactic	1.9	0.5
Total	4.0	3.1

Notes. The count rates are given in units of 10^{-4} cts/s per PSF HEW for 7 telescopes. The extragalactic component accounts for unresolved sources only, at the average four year survey sensitivity (Table 2).

The eROSITA[2] telescope (extended ROentgen Survey with an Imaging Telescope Array) will be able to statisfy this demand. It is the main instrument aboard the Russian Spektrum-Roentgen-Gamma satellite which is scheduled for launch in 2014. Its main science goals are cosmologi-

[1] http://www2011.mpe.mpg.de/xray/wave/rosat/

[2] http://www.mpe.mpg.de/eROSITA

Table 2. Characteristic average parameters of the eROSITA all-sky survey.

Survey duration	4.0 years				0.5 years	
Sky region	Extragalactic sky		Ecliptic poles		Extragalactic sky	
Solid angle [$\deg^2$]	$\sim 34\,100$		~ 90		$\sim 34\,100$	
Exposure time [sec]	2 000		20 000		260	
Energy band [keV]	$0.5-2.0$	$2-10$	$0.5-2.0$	$2-10$	$0.5-2.0$	$2-10$
Resolved extrag. CXB [%]	31	6	53	17	12	$\lesssim 1$
Background counts [cts/PSF]	0.8	0.6	6.7	6.1	0.1	0.1
Source counts [cts/PSF]	7.6	6.8	16.5	15.6	4.4	3.9
Sensitivity $\langle S_{\rm lim}\rangle$ [erg s^{-1} cm^{-2}]	1.1×10^{-14}	1.8×10^{-13}	2.3×10^{-15}	4.2×10^{-14}	4.8×10^{-14}	8.0×10^{-13}
Source density [deg^{-2}]	84	3.7	450	37	10.0	0.4
Number of sources [$\times10^3$]	$\sim 2\,900$	~ 130	~ 41	~ 3.4	~ 340	~ 13

cal studies with clusters of galaxies and active galactic nuclei, aimed to constrain the nature of dark matter and dark energy. To achieve these goals, eROSITA will perform an all-sky survey (eRASS) during the first four years of its operation, followed by a phase of pointed observations. Main parameters of the mission and the telescope are described in the eROSITA Science Book (Merloni et al. 2012, hereafter SB).

In this study we explore the main statistical properties of the AGN sample to be detected in the course of the eRASS, including their luminosity and redshift distributions. This will help to understand the capabilities of the eROSITA mission and, potentially, to tune the survey strategy and its parameters. Our work will complement the study about AGN presented in the SB.

Throughout the paper we use the following cosmological parameters: $H_0 = 70.0\,{\rm km\,s^{-1}\,Mpc^{-1}}$, $\Omega_m = 0.30$, $\Omega_\Lambda = 0.70$, $\Omega_k = 0$. These values are commonly used for XLF modeling of AGN and are in a reasonable agreement (within 2σ) with the recent results of the WMAP mission (Komatsu et al. 2011). We use the decimal logarithm throughout the paper. The calculations are performed for two energy bands – soft ($0.5-2.0$ keV) and hard ($2.0-10.0$ keV). In computing count rates we used the most recent response matrix of eROSITA, `erosita_iv_7telfov_ff.rsp`[3]. As it is appropriate for the all-sky survey data analysis, this response matrix is averaged over the field of view and scaled to 7 telescopes. In this work, we assume that the data from the entire survey of eROSITA is available for analysis.

2. Sensitivity

The point source detection sensitivity of eROSITA in the all-sky survey was discussed in detail by Prokopenko & Gilfanov (2009). Since then, the spacecraft orbit has been changed to the L2 orbit and detailed calculations of the instrumental background became available. We therefore update the calculations of Prokopenko & Gilfanov (2009) below.

2.1. Instrumental and cosmic background

The eROSITA background is dominated by the photon background below ~ 2 keV and by the particle component above this energy. In the further calculations we will use the field of view averaged angular resolution (PSF half energy width) of $30''$ diameter for the soft band and $40''$ diameter in the hard band (Friedrich et al., priv. comm.). The corresponding PSF HEW areas are ~ 707 and $\sim 1\,257\,{\rm arcsec}^2$, respectively. For the eRosita focal length, 1 mm on the detector corresponds to ≈ 128.8 arcsec.

The instrumental non X-ray (particle) background has a nearly flat spectrum in the counts space, with the normalization of $\approx 6.1\times10^{-3}\,{\rm cts\,s^{-1}\,cm^{-2}\,keV^{-1}}$ (Perinati et al. 2012). Within the PSF HEW it produces the count rates of 2.7×10^{-5} and 2.6×10^{-4} cts/s for the soft and hard band respectively, for 7 telescopes. Solar activity induced background events are not taken into account in this calculation, they are roughly accounted for via the observing efficiency introduced in the survey exposure time calculations. It should be realized that these numbers are a result of a purely theoretical calculations and no direct measurements of the real background of a X-ray detector in the L2 orbit exist. Therefore the above numbers may have to be revised after the eROSITA launch.

The X-ray photon background has two components (Lumb et al. 2002): (1) the truly diffuse galactic background due to local ionized ISM with a soft thermal spectrum and (2) the hard power-law extragalactic CXB component.

For the contribution of the ionized ISM emission we used the spectral fits from Lumb et al. (2002, Table 3) and obtained a count rate of 1.8×10^{-4} cts/s within the PSF HEW for the soft band, assuming the same galactic absorption ($N_{\rm H} = 1.7\times10^{20}\,{\rm cm^{-2}}$) and solar abundance (Anders & Grevesse 1989) as Lumb et al. (2002). Its contribution to the hard band can be neglected. As a caveat we note that Lumb et al. (2002) analysis was based on the XMM-Newton observations of several blank fields located at high galactic latitudes. Therefore the above numbers should be considered as approximate, as they do not account for inhomogeneity of the galactic background radiation.

For the extragalactic CXB component we assume a power-law spectrum with the photon index of $\Gamma = 1.42$ (Lumb et al. 2002, Table 3). The power-law was normalized to the extragalactic CXB flux of 7.53×10^{-12} and $2.02\times10^{-11}\,{\rm erg\,s^{-1}\,cm^{-2}\,deg^{-2}}$ for the soft and hard band

[3] `http://www2011.mpe.mpg.de/erosita/response/`

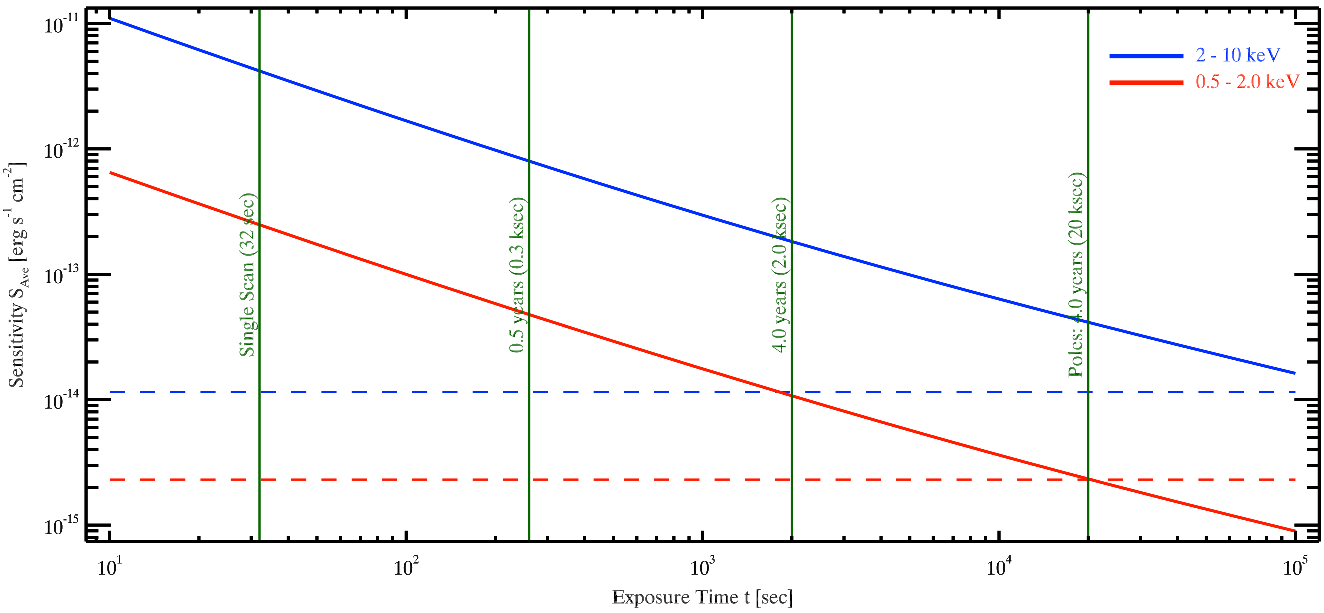

Fig. 1. The average point source detection sensitivity of the eROSITA telescope as a function of the exposure time in the soft (*red*) and hard (*blue*) energy bands for the extragalactic sky. The horizontal dashed lines are the confusion limits for 1 sources per 40 telescope beams (PSF HEW). The vertical line on the left shows exposure time for a single scan at 100 % observing efficiency and the other vertical lines indicate the average exposure times for different survey durations and at the ecliptic poles (for the soft band confusion limit) at 80 % observing efficiency.

(Moretti et al. 2003)[4]. We will further assume galactic absorption of $N_{\mathrm{H}} = 6 \times 10^{20}\,\mathrm{cm}^{-2}$ corresponding to the arithmetic mean of the N_{H}-map of Kalberla et al. (2005) for the extragalactic sky ($|b| > 10°$). With these parameters, the average count rate due to extragalactic CXB within the PSF HEW (7 telescopes) is 2.8×10^{-4} and 5.8×10^{-5} cts/s in the soft and hard band respectively.

In computing the contribution of extragalactic sources, one needs to take into account that a fraction of background AGN will be resolved by eROSITA. Therefore, these sources will not contribute to the unresolved image background, affecting the point source detection sensitivity. This effect leads to a reduction of the extragalactic background count rate. At the average four year survey sensitivity of eROSITA (Table 2) the resolved extragalactic CXB fraction[5] achieves $\sim 31\,\%$ in the soft and $\sim 6\,\%$ in the hard band. The fractions were calculated by using the number counts of Georgakakis et al. (2008, hereafter G08) and the extragalactic CXB flux of Moretti et al. (2003). Thus, the final values of the average count rate of unresolved CXB emission within the PSF HEW is 1.9×10^{-4} and 5.4×10^{-5} cts/s in the soft and hard bands respectively.

The contributions of different background components are summarized in the Table 1. They are consistent within $\sim 10\,\%$ with the numbers in the SB. The difference in the soft band comes from the slight difference in the normalization of the extragalactic component. The change in the hard band is caused by the fact, that we use the results of updated calculations of particle background of Perinati et al. (2012), instead of Tenzer et al. (2010) used in the SB.

[4] Strictly speaking, these flux values correspond to slightly steeper slope (≈ 1.45) of the CXB spectrum than the conventional value of 1.42. This discrepancy reflects the uncertainty in the absolute CXB flux determinations. We will nevertheless use them for consistency with the resolved fraction calculations later in this paragraph.

[5] Note that the Fig.5 in Moretti et al. (2003) gives resolved fractions of $\sim 50\,\%$ and $\sim 10\,\%$ respectively. This difference also reflects the uncertainties of the CXB measurements.

2.2. Average exposure and sensitivity

With the average background count rates we compute the point source detection sensitivity of eROSITA as a function of the exposure time, which is shown in Fig. 1. In this computation we assumed Poissonian distribution of counts and demand no more than 200 false point source detections for the entire sky. This corresponds to one false detection in ~ 250 fields of view ($\sim 210\,\mathrm{deg}^2$). For a Gaussian distribution, this false detection rate is equivalent to a $\sim 5.0\sigma$ confidence level in one trial. In converting the count rates to flux we assume an absorbed power-law spectrum with the photon index $\Gamma = 1.9$ and the sky-averaged galactic absorption of $N_{\mathrm{H}} = 6 \times 10^{20}\,\mathrm{cm}^{-2}$. We also take into account that only half of the source counts are contained within the PSF HEW.

The sky-averaged exposure time of the survey is:

$$t_{\mathrm{exp}} \approx 2.0 \left(\frac{t_{\mathrm{survey}}}{4\,\mathrm{years}}\right) \left(\frac{f_{\mathrm{eff}}}{80\,\%}\right) \left(\frac{\mathrm{FOV}}{0.833\,\mathrm{deg}^2}\right) \mathrm{ksec}\ , \quad (1)$$

where t_{survey} is the survey duration, and $f_{\mathrm{eff}} = 80\,\%$ is the observing efficiency. Here we assumed the eROSITA field of view of 1.03° (diameter). The average numbers of background counts to be accumulated within PSF HEW in the course of the 4 years survey (average exposure time of 2.0 ksec per point) are: ~ 0.8 and ~ 0.6 in the soft and hard bands. For these numbers and for the chosen confidence level, the source detection thresholds are ~ 8 and ~ 7 source counts within the PSF HEW. The corresponding point source detection sensitivities are $\langle S_{\mathrm{lim}} \rangle \approx 1.1 \times 10^{-14}$ and $\approx 1.8 \times 10^{-13}\,\mathrm{erg\ s}^{-1}\,\mathrm{cm}^{-2}$ in the soft and hard bands respectively.

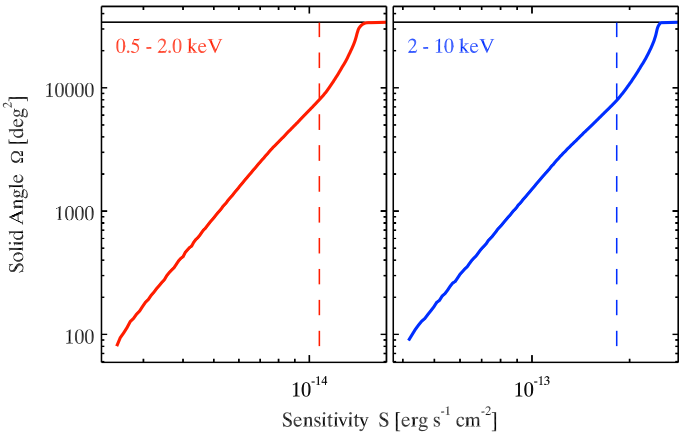

Fig. 3. The sensitivity – solid angle curves for the soft (*left panel*) and hard (*right*) bands. The vertical dashed lines show the corresponding average sensitivities from the Table 2. The horizontal line shows the solid angle of the extragalactic sky.

After the first half a year, eROSITA will have scanned once the whole sky. At the averaged exposure time of ∼ 260 sec, there will be ∼ 0.1 background counts per PSF HEW in each energy band and the point source detection threshold will be ∼ 4 counts. The point source detection limits for the half year survey are $\sim 4.8 \times 10^{-14}$ and $\sim 8.0 \times 10^{-13}\,\mathrm{erg\,s^{-1}\,cm^{-2}}$, respectively.

Main characteristics of the full survey and its first half a year are summarized in the Table 2. These numbers are generally consistent with the SB. The small difference are related the differences in the background estimates and the larger PSF size used for the hard band. Also, we iteratively calculate the resolved fraction of the extragalactic CXB for sensitivities.

Thus, the eRASS will have in average a ∼ 30 times better sensitivity in the soft band than the previous all-sky survey in this band, conducted by ROSAT (Voges et al. 1999). On the other hand, its sensitivity is ∼one to ∼four orders of magnitude lower than that of the deep, but much more narrow, (some of them pencil-beam) extragalactic X-ray surveys conducted by *Chandra* and XMM-Newton, e.g. CDFs, COSMOS, Bootes, Lockman Hole, ChaMP etc (see Brandt & Hasinger 2005, for a review).

2.3. Confusion limit

For the purpose of this study we assume that the source confusion becomes of importance at the source density of 1 sources per 40 telescope beams (= PSF HEW) which for the angular resolution of eROSITA corresponds to the source density of ∼ 460 and ∼ 260 sources $\mathrm{deg^{-2}}$ in the soft and hard band. With the average of the extragalactic $\log N - \log S$ curves of G08 and Kim et al. (2007, Table 3, ChaMP+CDFs, hereafter K07) the corresponding flux levels are $\sim 2.3 \times 10^{-15}$ and $\sim 1.2 \times 10^{-14}\,\mathrm{erg\,s^{-1}\,cm^{-2}}$. In the soft band the confusion limit is achieved at the exposure time of ∼ 20 ksec. In the hard band, source confusion, achieved at the exposure time of ∼ 190 ksec, is not an issue for eRASS.

2.4. Sensitivity map

Due to the properties of the scan pattern, the two ecliptic poles of eROSITA will have a significantly higher exposure time than the sky on average (see the SB for more details). This leads to a higher sensitivity at the ecliptic poles. The scan strategy of eROSITA is still under discussion and different scenarios are still possible, depending on whether the satellite rotation axis is continuously pointing at the Sun or moves around it with a slight offset. In the latter scenario, the ecliptic pole regions will occupy smaller solid angle and will be less overexposed. We consider here the extreme case of the continuous Sun pointing of the scan axis.

Using the exposure map of the four-year survey (Robrade, priv. comm.), we define the two sky regions at the ecliptic poles of eROSITA, where the exposure time exceeds the confusion limit of 20.0 ksec. These two pole regions combined cover the solid angle of $\sim 90\,\mathrm{deg^2}$. The point source detection sensitivity in the soft band in the pole regions is defined by the confusion limit and is approximately $\sim 2.3 \times 10^{-15}\,\mathrm{erg\,s^{-1}\,cm^{-2}}$, taking into account ∼ 50 % resolved CXB fraction. The survey characteristics for the pole regions are summarized in Table 2. In the hard band, the confusion limit is reached at much longer exposure time of ∼ 190 ksec and is not relevant for the all-sky survey. The actual hard band sensitivity in the pole regions is determined by the particular scan pattern. For the reference, we give in the Table 2 the sensitivity which can be achieved in the hard band assuming the 20 ksec exposure.

Outside the poles, exposure time still varies significantly with the minimal value of ∼ 1.6 ksec achieved in the equatorial regions. These variations will lead to variations of the point source detection sensitivity across the sky. To compute a realistic sensitivity map of the survey, along with the exposure map we take into account variations of the galactic absorption across the sky. To this end we use the N_{H}-map of Kalberla et al. (2005). We exclude the galactic plane and only consider the sky at galactic latitudes $|b| > 10°$ for further calculations. The solid angle of the so defined extragalactic sky is $\Omega \approx 34\,100\,\mathrm{deg^2}$, which corresponds to ≈ 83 % of the total sky. For the extragalactic sky the arithmetic mean of the N_{H}-map is $\langle N_{\mathrm{H}} \rangle \approx 6 \times 10^{20}\,\mathrm{cm^{-2}}$ and of the exposure map ∼ 2.1 ksec, which is close to the average exposure time given by Eq. (1). For the exposure map we assumed the observing efficiency of $f_{\mathrm{eff}} = 80\,\%$ and set overexposed regions to 20.0 ksec. These areas correspond to the ecliptic poles defined above.

For the background calculation, we assume the constant count rate for the particle background. We assume that the soft galactic background is produced in the Local Bubble and therefore is not subject to galactic absorption. Furthermore, we ignore its dependence on the sky direction assuming the count rate derived in the previous subsections. In computing the count rate due to unresolved part of the extragalactic background, we take the N_{H}-map into account but fix the resolved fraction of CXB at the sky-averaged value.

With these assumptions we compute the sensitivity map, shown in Fig. 2. The sensitivity – solid angle dependences are shown in Fig. 3.

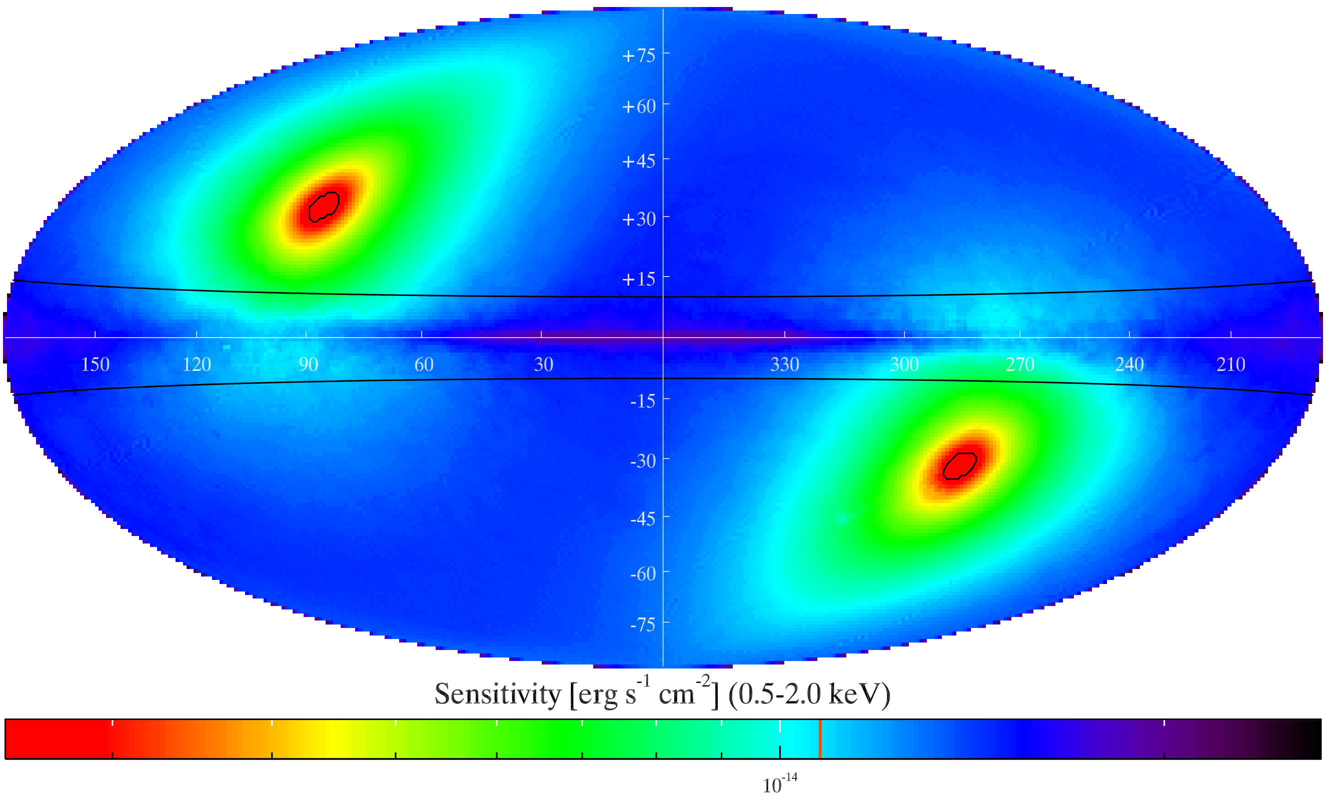

Fig. 2. The four year soft band sensitivity map of eRASS in galactic coordinates (l, b), based on the exposure time map of Robrade (priv. comm.) for a continuous Sun pointing and on the N_{H}-map of Kalberla et al. (2005). The two black horizontal curves enclose the galactic plane ($|b| < 10°$), which is excluded in our calculation, and the two regions encircled by black curves are our defined ecliptic poles, where the exposure time was set to 20.0 ksec. The red vertical line in the horizontal color bar shows the average sensitivity (from Table 2).

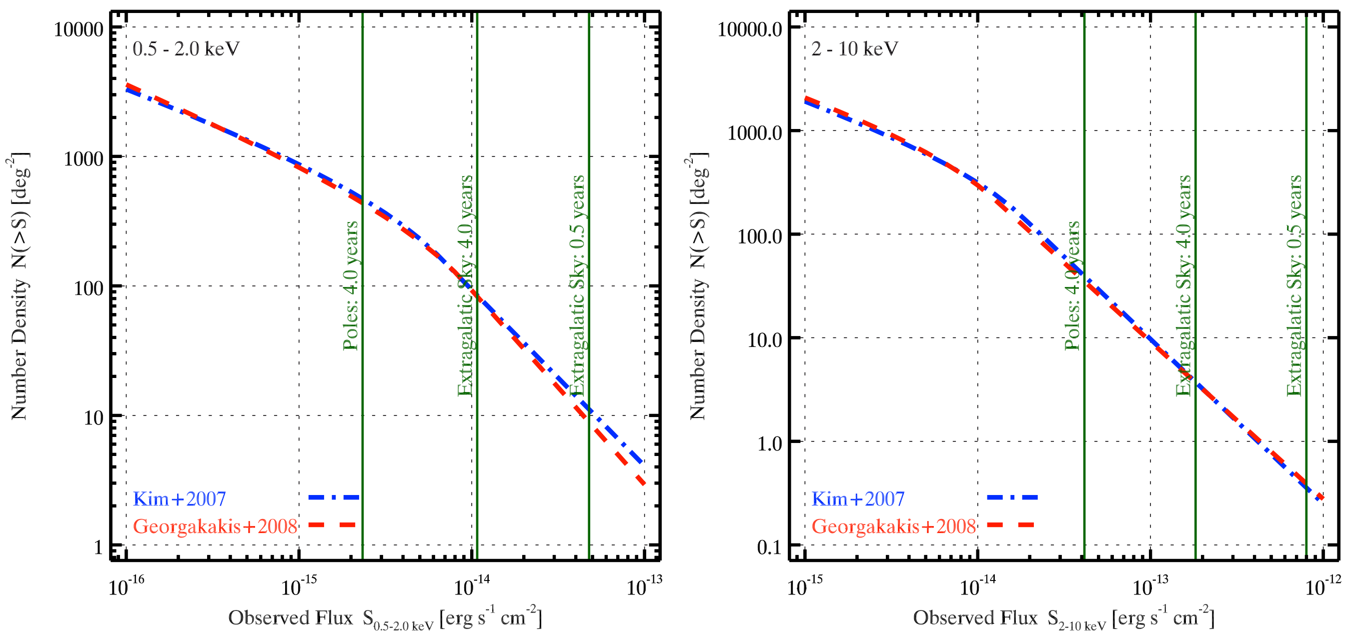

Fig. 4. The cumulative number counts $N(>S)$ for observed X-ray point sources in the soft band (*left*) and hard band (*right*). The blue, dashed-dotted curve is for Kim et al. (2007, Table 3, ChaMP+CDFs) and the red, dashed curve is for Georgakakis et al. (2008). The vertical solid lines indicate the point source detection sensitivity for different survey durations assuming 80 % observing efficiency, and the sensitivity at the 20 ksec exposure time, corresponding to the confusion limit in the soft band (leftmost line marked "Poles").

3. The AGN number counts

In order to estimate the source densities and the total numbers of sources detected in different bands we use the source counts results of K07 and G08, displayed in Fig. 4. For K07, we used the best-fit parameters for the ChaMP+CDFs data from their Table 3 and converted the break flux ($S_{\rm b}$) in the hard band from $2.0-8.0$ keV to $2.0-10.0$ keV assuming a power-law spectra with a photon index of $\Gamma=1.4$ as it was used by K07. The best-fit parameters of K07 and G08 are in a good agreement (within 2σ). The difference in number counts between the two $\log N-\log S$ curves is mostly below 10 % with a maximum deviation of $\sim 20\%$ in the flux range of interest (defined by the characteristic sensitivities, see Table 2). In the following calculations we use the average of the values given by the two $\log N-\log S$ curves.

With these curves and our sensitivity map in each energy band, we compute the number density map. The arithmetic mean of this map give us the average number density of $\sim 81\,\deg^{-2}$ and $\sim 3.8\,\deg^{-2}$ in the soft and hard band, respectively. The total numbers of sources detected are $\sim 2.7\times10^6$ and $\sim 1.3\times10^5$ for the extragalactic sky. These values differ slightly from those in Table 2 because the latter were computed using average sensitivities of the survey. They are in a reasonable agreement with those in the SB. About $\sim 10\,\%$ of these sources in both bands will be detected after the first half a year of the survey.

For the ecliptic poles, taking the corresponding sensitivities from Table 2, we compute a number density of $\sim 450\,\deg^{-2}$ and $\sim 37\,\deg^{-2}$ in the soft and hard band, respectively. This translates in $\sim 41\,000$ and $\sim 3\,400$ detected extragalactic point sources after four years.

About 10 % of the brightest AGN in eRASS will be detected with at least ~ 38 and ~ 30 counts per PSF HEW (corresponding flux limits 5.4×10^{-14} and 8.0×10^{-13} erg s^{-1} cm^{-2}) in the soft and hard band respectively. The 10 % faintest AGN will have around ~ 8 and ~ 7 counts per PSF HEW (1.2×10^{-14} and 2.0×10^{-13} erg s^{-1} cm^{-2}).

We use the sensitivity map to estimate the numbers of AGN to be detected in the galactic plane, $|b|<10^\circ$ and obtain $\sim 4.6\times10^5$ and $\sim 2.2\times10^4$ sources. This is somewhat smaller than predicted using the average source density on the extragalactic sky ($\sim 6.0\times10^5$ and $\sim 2.7\times10^4$) since the galactic absorption in the galactic plane is on average an order of magnitude higher than for the extragalactic sky. The higher galactic X-ray background, not accounted for in these calculations, will further reduce the number of AGN at low galactic latitudes and high confusion with galactic sources will make their identifications more difficult.

Finally, we note that AGN will be the most abundant source in eRASS. Apart from them, eRASS will detect about $\sim 10^5$ galaxy clusters (Predehl et al. 2010), $\sim 2\times10^4$ normal galaxies (Prokopenko & Gilfanov 2009) and $\sim 4\times10^5$ stars (Merloni et al. 2012).

4. The X-ray luminosity function of AGN

With the knowledge of the X-ray luminosity function (XLF) of AGN,

$$\phi(L,z)=\frac{\mathrm{d}\Phi(L,z)}{\mathrm{d}\log L} \tag{2}$$

we are able to compute the redshift and luminosity distributions of the AGN to be detected in eRASS. The XLF describes the number of AGN (N) per unit co-moving volume (V) and logarithmic X-ray luminosity ($\log L$) as a function of X-ray luminosity L and redshift z. It is currently believed that the luminosity-dependent density evolution (LDDE) model describes best the shape of the observed XLF (Miyaji et al. 2000; Ueda et al. 2003; Hasinger et al. 2005; Silverman et al. 2008; Ebrero et al. 2009). For completeness, we summarize it below. The LDDE model parameterizes the AGN XLF has a double power-law

$$\phi(L,z)=K_0\,\left[\left(\frac{L}{L_*}\right)^{\gamma_1}+\left(\frac{L}{L_*}\right)^{\gamma_2}\right]^{-1}\,e(L,z) \tag{3}$$

with the density evolution factor given by

$$e(L,z)=\begin{cases}(1+z)^{p_1} & z\le z_{\rm c}(L)\\ (1+z_{\rm c}(L))^{p_1}\,\left(\dfrac{1+z}{1+z_{\rm c}(L)}\right)^{p_2} & z>z_{\rm c}(L)\end{cases} \tag{4}$$

where the cut-off redshift is given by

$$z_{\rm c}(L)=\begin{cases}z_{\rm c,0}\,\left(\dfrac{L}{L_\alpha}\right)^{\alpha} & L\le L_\alpha\\ z_{\rm c,0} & L>L_\alpha\end{cases} \tag{5}$$

The so defined LDDE model has nine parameters. Miyaji et al. (2000) have a slightly different definition of the density evolution factor (Eqs. 4 and 5) for the soft band XLF, but the concept remains the same. Hasinger et al. (2005) used the luminosity dependent density evolution indices (p_1 and p_2)

$$p_1(L)=p_{1_{44}}+\beta_1\,(\log L-44.0) \tag{6}$$
$$p_2(L)=p_{2_{44}}+\beta_2\,(\log L-44.0) \tag{7}$$

and therefore the number of parameters increases with the two additional parameters (β_1 and β_2) up to eleven.

As our default XLF models we used the LDDE model of Hasinger et al. (2005, Table 5, hereafter H05) for the soft band and of Aird et al. (2010, hereafter A10) for the hard band. For the hard band XLF we used the best fit model from A10, the "color preselected sample" (their Table 4), which should provide a more accurate description of the XLF at higher redshifts. The parameters of the chosen XLF models are summarized in the Table 3.

Based on the XMM-Newton data, Brusa et al. (2009) demonstrated that the soft band XLF of H05 overpredicts the numbers of high redshift objects, $z>3$, detected in the COSMOS survey. They proposed to introduce an exponential redshift cutoff of the XLF for $z>2.7$,

$$\phi=\phi_{\rm H05}(z\!=\!2.7)\,\times\,10^{0.43\,(2.7-z)},\qquad z>2.7 \tag{8}$$

and showed that with this modification, the observed number counts of high redshift AGN are reproduced much better. This result was further confirmed by Civano et al. (2011), who used additional *Chandra* data on the same field and analyzed a $\sim 50\,\%$ bigger AGN sample than Brusa et al. (2009), and by Hiroi et al. (2012), who analyzed 30 high-redshift ($z>3$) AGN in the Subaru/XMM-Newton Deep Survey field. Introducing the redshift cutoff results in an insignificant, $\sim 1\,\%$, decrease in the total number of AGN above the eRASS sensitivity limit. However, it has a strong effect on the numbers of high redshift objects,

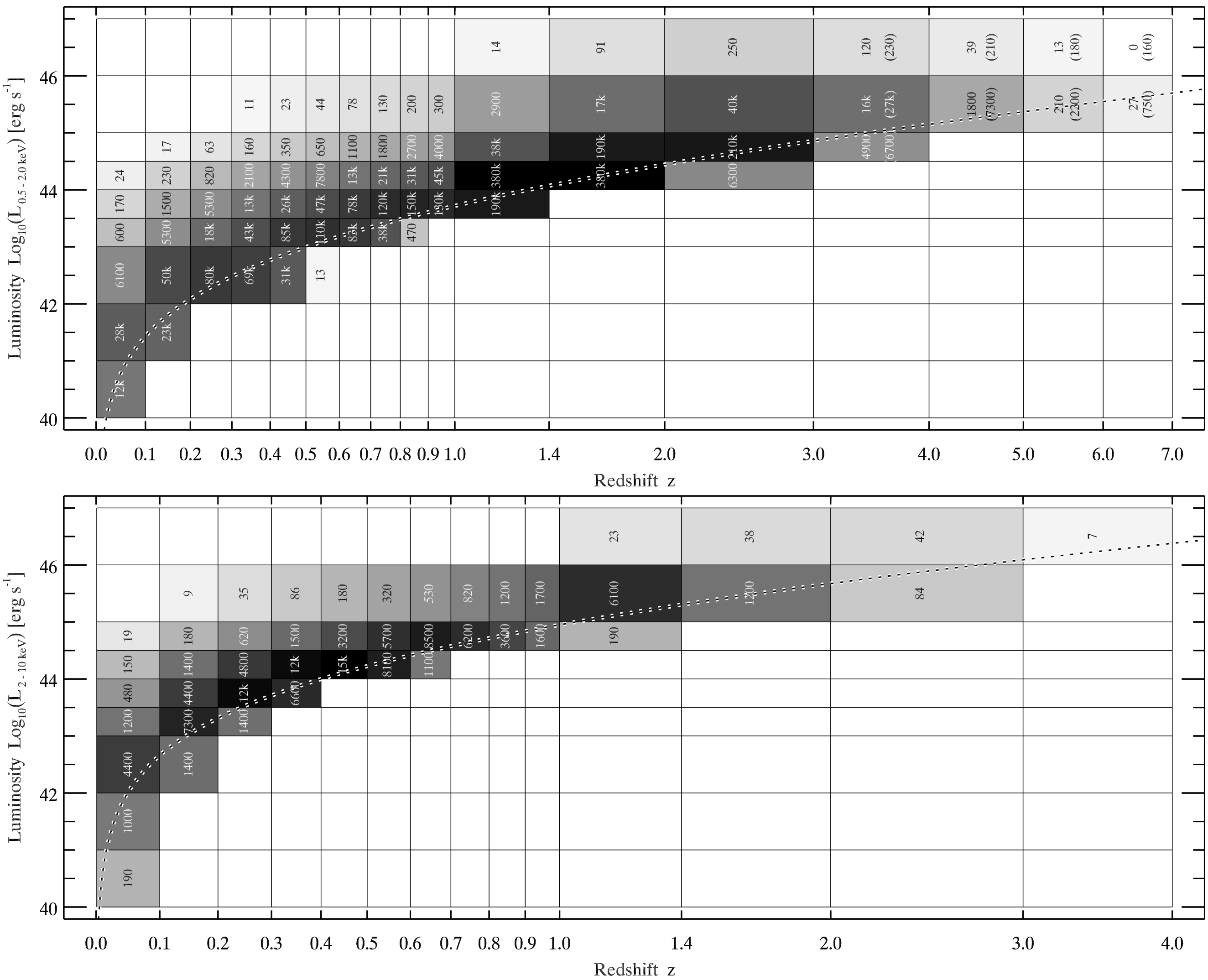

Fig. 5. The number of AGN in different redshift and luminosity bins to be detected in the course of the 4 year survey in the soft (*top*) and hard (*bottom*) bands. White empty bins with no number correspond to zero sources. The dotted line corresponds to the detection limit of eRASS. In the soft band plot, the numbers in brackets are for the XLF without the exponential redshift cut-off, they are given only if the difference exceeds 10 %.

which we will discuss in Sect. 5.4. For our default XLF in the soft band, we will include the high redshift cut-off described by the Eq. (8), but will additionally show results without such cutoff.

As a consistency check, we compute the $\log N - \log S$ distributions based on the chosen XLF models and compare with the results of the source counts by K07 and G08. The $\log N - \log S$ can be computed by integrating the XLF over luminosity L and redshift z:

$$N(>S) = \int_{0}^{z_{\max}} \frac{\mathrm{d}V(z)}{\mathrm{d}z} \int_{\log L_{\min}(S,z)}^{\log L_{\max}} \phi(\log L, z)\, \mathrm{d}\log L\ \mathrm{d}z \quad (9)$$

Here, $\frac{\mathrm{d}V(z)}{\mathrm{d}z}$ [$\mathrm{Mpc}^3\,\mathrm{sr}^{-1}$] is the co-moving volume element per redshift and solid angle[6] and $L_{\min}(S,z) = 4\pi\, S\, d_{\mathrm{L}}^2(z)$, where $d_{\mathrm{L}}^2(z)$ is the luminosity distance (e.g. Hogg 1999). K-correction is applied, assuming a power-law spectra with the photon index $\Gamma = 1.9$ and no absorption. The same photon index was used to convert the XLFs to the energy bands used in this paper, if the former was determined for a different energy band. It is worth to mention that deep X-ray surveys do not show any evidence of a redshift dependent photon index (Brandt & Hasinger 2005).

In the Eq. (9) as well as in the calculations described in the next sections, we integrate the XLF model in the luminosity range of $40 \leq \log L[\mathrm{erg\,s^{-1}}] \leq 48$ and in the redshift range of $0 \leq z \leq 7$. Decrease of the $L_{\min}$ in the luminosity integration or increase of the upper limit for the redshift integration, does not have any significant effect on the number counts $N(>S)$ in our flux range of interest. We should note, that all experimental XLF determinations are based on AGN samples, which cover a smaller luminosity range, typically $L \geq 10^{42}\,\mathrm{erg\,s^{-1}}$, and smaller redshift range ($z_{\max} \sim 3-5$). Hence, our calculations involve some extrapolation of the measured XLFs to lower luminosities and higher redshift. The uncertainties introduced by this extrapolation are generally small, with a few exceptions which are discussed below.

[6] The solid angle is converted from steradian to square degrees ($\pi^2\,\mathrm{sr} = 180^2\,\mathrm{deg}^2$).

Table 3. Parameters of the LDDE model used to compute the luminosity and redshift distributions of the detected AGN.

Energy band [keV] XLF	0.5 − 2.0 H05 (Table 5)	2 − 10 A10 (Table 4)
K_{44} / K_0 [(a)]	2.62 ± 0.16 [(b)]	8.32 ± 1.15
$\log L_*$ [(c)]	43.94 ± 0.11	44.42 ± 0.04
γ_1	0.87 ± 0.10	0.77 ± 0.01
γ_2	2.57 ± 0.16	2.80 ± 0.12
$p1_{44}$ / p_1	4.7 ± 0.3 [(d)]	4.64 ± 0.24
$p2_{44}$ / p_2	-1.5 ± 0.7 [(d)]	-1.69 ± 0.12
$z_{c,44}$ / $z_{c,0}$	1.42 ± 0.11 [(e)]	1.27 ± 0.07
$\log L_\alpha$ [(c)]	44.67 (fixed)	44.70 ± 0.12
α	0.21 ± 0.04	0.11 ± 0.01
β_1	0.7 ± 0.3	–
β_2	0.6 ± 0.8	–

Notes. [(a)] In units of $10^{-7}\,\mathrm{Mpc}^{-3}$. [(b)] $K_0 = K_{44}\,[(10^{44.0}/L_*)^{\gamma_1} + (10^{44.0}/L_*)^{\gamma_2}] \approx 6.69$. [(c)] erg s^{-1}. [(d)] p_1 and p_2 are computed from the Eqs. (6) and (7). [(e)] $z_{c,0} = z_{c,44}\,10^{\alpha\,(\log L_\alpha - 44.0)} \approx 1.96$.

For the soft band counts, using the XLF of H05 we predict somewhat smaller number of AGN that observed by K07 and G08, with a maximum deviation of $\sim 30-50\,\%$ for the $\log N - \log S$ curve in our flux range of interest. A part of this discrepancy is due to the fact that H05 selected only Type 1 AGN, and a part may be due the cosmic variance. As it is beyond the scope of this work to investigate the origin of this difference in detail we renormalized the soft band XLF of H05 upwards with a factor of ~ 1.35 in order to match the source counts of K07 and G08 in the flux range of interest. The hard band $\log N - \log S$ obtained using the XLF of A10 agrees well with the observed source counts, with a maximum deviation of $\sim 3 - 11\,\%$ in the flux range of interest.

5. Luminosity and redshift distribution of detected AGN

With the knowledge of the XLF (Sect. 4) we can compute luminosity and redshift distributions of detected AGN as follows:

$$\frac{\mathrm{d}N(L)}{\mathrm{d}\log L} = \int\limits_0^{z_{\max}(S,L)} \phi(\log L, z)\,\frac{\mathrm{d}V(z)}{\mathrm{d}z}\,\mathrm{d}z \qquad (10)$$

$$\frac{\mathrm{d}N(z)}{\mathrm{d}z} = \frac{\mathrm{d}V(z)}{\mathrm{d}z} \int\limits_{\log L_{\min}(S,z)}^{\log L_{\max}} \phi(\log L, z)\,\mathrm{d}\log L \qquad (11)$$

where $z_{\max}$ is defined by the relation $d_{\mathrm{L}}(z_{\max}) = \sqrt{L/(4\pi S)}$, where $d_{\mathrm{L}}(z_{\max})$ is the luminosity distance at the redshift $z_{\max}$. For the other quantities and the K-correction see the explanation after the Eq. (9). The corresponding cumulative distributions are:

$$N(>L) = \int\limits_L^{L_{\max}} \mathrm{d}N(L') \qquad (12)$$

$$N(>z) = \int\limits_z^{z_{\max}} \mathrm{d}N(z') \qquad (13)$$

The distribution of the AGN detected in the eRASS over the luminosity and redshift is summarized in the Fig. 5 and is further discussed in the next two subsections. In computing these distributions we took into account the sensitivity map (Sect. 2.4) of the eRASS via the sensitivity – solid angle distribution shown in Fig. 3. For the overexposed areas at the ecliptic poles we used the sensitivity quoted in Table 2. The properties of the 10 % of brightest and faintest objects we computed using the flux limits from Sect. 3.

5.1. Luminosity distribution

Luminosity distributions of detected AGN are shown in the Fig. 6. In the soft band they peak at $\log L \sim 44$, with the little difference between the extragalactic sky sample ($\log L \sim 44.0$) and the ecliptic poles ($\log L \sim 43.8$). The peak in the hard band is at $\log L \sim 44.4$. The median values differ by less than 1 % from the corresponding peak values. Comparing with the values of L_* from the Table 3, we can see that the location of the peak is defined by the L_* luminosity and does not strongly depend on the survey sensitivity. A change of the latter by two orders of magnitude changes the position of the peak only by ~ 0.5 dex. Hence, our predictions for the luminosity distribution are rather robust against moderate changes of the survey sensitivity. From the top panel of Fig. 6 one can see that the luminosity distribution in the soft band changes only marginally at high luminosity, if we do not include the high-redshift cutoff of the XLF.

From the cumulative luminosity distributions of the extragalactic sky (right panels of Fig. 6) we can see that about 10 % (vertical dashed lines) of the detected AGN will have luminosities higher than $\sim 10^{45}$ erg s^{-1}. This large sample of luminous AGN ($\sim 3 \times 10^5$ in total) will improve constrains on the high-luminosity end of the XLF. For comparison, the AGN sample of H05 had about ~ 100 AGN with a luminosity higher than $\sim 10^{45}$ erg s^{-1}.

In the top panel of Fig. 8, we can see that the luminosity distribution of the 10 % brightest (blue curve) and 10 % faintest (red) AGN do not differ much from each other and from that of the total sample (black). We note that the luminosity distribution of objects detected in a half a year survey is well represented by that of the 10 % brightest sources.

5.2. Redshift distribution

Unlike the luminosity distributions, redshift distributions of a flux limited sample are strongly dependent on the limiting flux (Fig. 7). Correspondingly, the redshift distributions for the extragalactic sky sample and for the poles peak at different redshift, the difference being larger for the hard band. The same is true for the median values, which are listed together with the peak values in Table 4. The median and

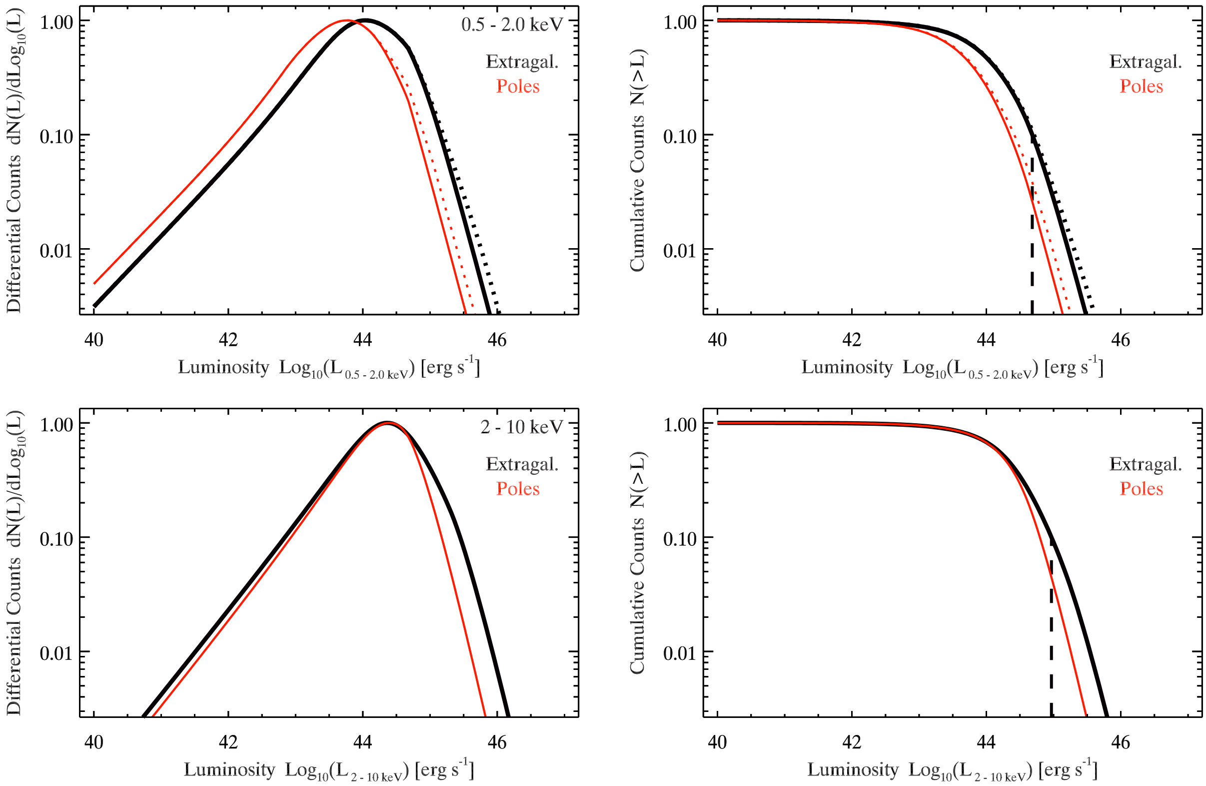

Fig. 6. The differential (*left*) and cumulative (*right*) luminosity distribution of AGN in the soft (*top*) and in the hard (*bottom*) band. The distributions are normalized to the unity, to facilitate comparison of the shapes. The dotted curves in the top panels were computed without the high redshift cutoff in the soft band XLF (see Sect. 4). The dashed black vertical lines in the right panels show the luminosity corresponding to the 10 % fraction of sources.

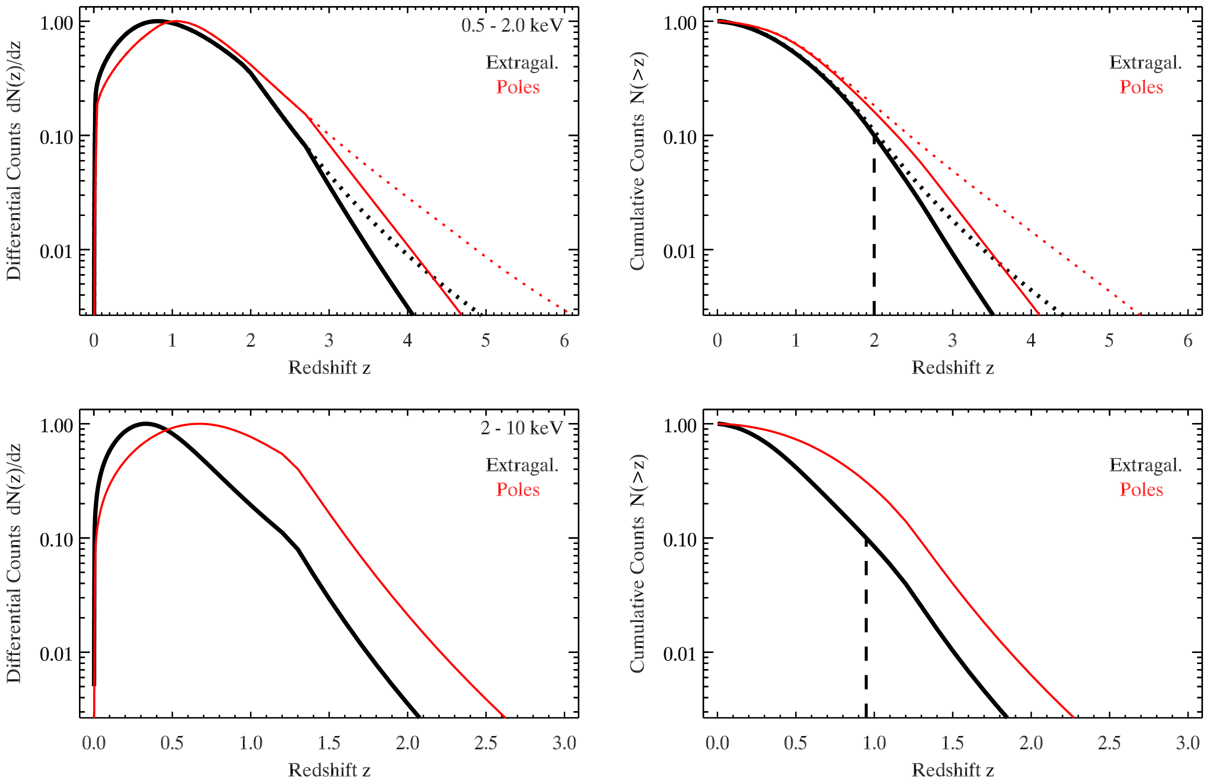

Fig. 7. Same as Fig. 6 but for the redshift distribution.

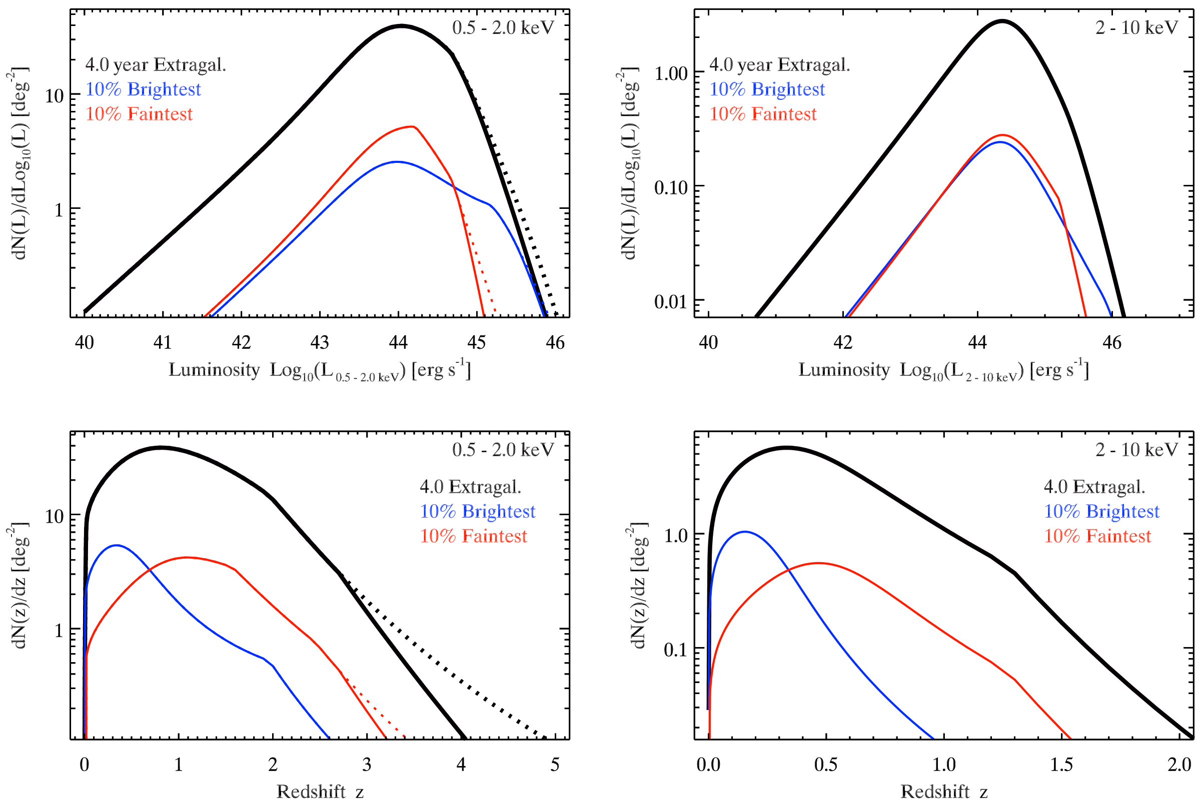

Fig. 8. The differential luminosity (*top*) and redshift (*bottom*) distributions in the soft (*left*) and hard (*right*) bands for the extragalactic sky sample after fours years (*black*) and for the 10 % brightest (*blue*) and 10 % faintest AGN (*red*).

Table 4. The peak and median values of the redshift distribution of eRASS AGN

	$0.5-2.0$ keV		$2-10$ keV	
	Peak	Median	Peak	Median
4.0 years Extragalactic	~ 0.8	~ 1.0	~ 0.3	~ 0.4
4.0 years Ecliptic Poles	~ 1.0	~ 1.2	~ 0.7	~ 0.7
10 % brightest	~ 0.3	~ 0.5	~ 0.2	~ 0.2
10 % faintest	~ 1.1	~ 1.2	~ 0.5	~ 0.5
0.5 years Extragalactic	~ 0.4	~ 0.6	~ 0.2	~ 0.2

peak values in the soft band do not change significantly, if we do not include the exponential high-redshift cutoff in our calculations. However, the redshift distribution of AGN at high redshift does change significantly, which we can see clearly in the top panel of Fig. 7. This will be discussed in more detail in Sect. 5.4.

The differential distributions show several breaks which are caused by the derivative discontinuities of the LDDE model. Another break at the low redshift, $z \sim 0$, appears when the low integration limit in Eq. (11), $\log L_{\min}(S,z)$, becomes equal to the low limit of the interval where the XLF is defined ($L = 10^{40.0}$ erg s^{-1}, Sect. 4). These features are non-physical and reflect the deficiencies of the functional form used in the LDDE model. However, these deficiencies of the XLF model do not compromise the overall shapes of the redshift (and luminosity) distributions derived in this paper, as long as the overall shape of the AGN X-ray luminosity function is adequately represented by the LDDE model.

In accord with the note made in the beginning of this section, redshift distributions of the 10 % brightest AGN and the 10 % faintest (Fig. 8) peak at significantly different redshifts than the overall distributions (black). Similar to luminosity distributions, the redshift distributions of the objects detected during a half a year survey are similar to the distributions of the 10 % brightest objects. From the cumulative distributions (right panels in the Fig. 7.) we conclude that in the soft band, $\approx 50\,\%$ of objects in the eRASS sample will be located at $z > 1$, whereas $\approx 10\,\%$ will be located at $z > 2$.

5.3. Uncertainties

Obviously, the accuracy of our predictions depends on the accuracy of the AGN XLF. The latter is limited by the rather moderate numbers of objects used for their construction, typically ~ 1000. Although the XLFs obtained by different authors are broadly consistent with each other, there still is considerable spread between different models. Correspondingly, using XLF models obtained by different authors we obtain somewhat varying luminosity and redshift distributions of eRASS AGN.

In order to illustrate the range of uncertainties, we calculated the luminosity and redshift distributions for the soft band extragalactic sky sample using several different XLF models available in the literature. Along with our default soft band XLF, we used the XLF of H05 without the exponential redshift cutoff and XLF models of Miyaji et al. (2000, Table 3) and Ebrero et al. (2009). These XLFs models are based on (overlapping) samples, each containing $\sim 10^3$ objects in total. As the samples

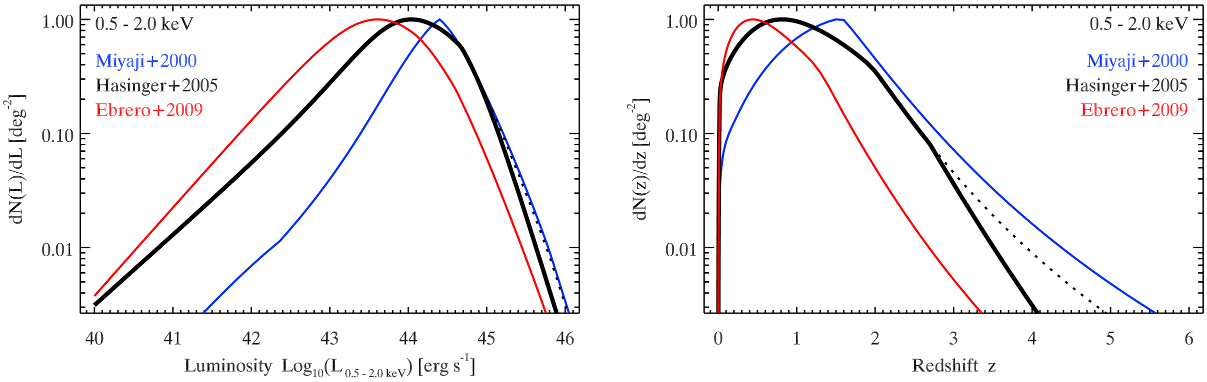

Fig. 9. The luminosity (*left*) and redshift (*right*) distributions of the soft band extragalactic sky sample computed using different XLFs. The thick solid black curve shows the prediction based on the default XLF model. Also shown are predictions for the XLF model of Miyaji et al. (2000, Table 3), Hasinger et al. (2005, Table 5, without the exponential redshift cutoff, dotted curve) and Ebrero et al. (2009). All the curves are normalized to unity.

partly overlap, these models are not entirely independent. Additional, Ebrero et al. (2009) applies a correction for absorption, which the others do not have and we do not include in our calculation. The resulting luminosity and redshift distributions of eRASS extragalactic sky sample are shown in the Fig. 9. In order to facilitate comparison of the shapes, the distributions are normalized to the unity.

Another factor is the cosmic variance. As the AGN XLF determinations rely on the survey covering only a small fraction of the sky, $\lesssim 10^{-4} - 10^{-3}$ at most, they are subject to cosmic variance. The amplitude of this uncertainty is probably in the $\sim 10\,\%$ range (Aird et al. 2010). Obviously, the eRASS sample will provide means for studying this effect in full detail.

We do not consider any seperation between different types of AGN. H05 only consider type 1 AGN for their XLF model. If we take into accout the expected small fraction ($\sim$ 10 % [7], see also Merloni et al. 2012) of type 2 AGN (intrinsic $N_{\rm H} > 10^{21}\,{\rm cm}^{-2}$) and the rather similar XLF of both types (e.g. Burlon et al. 2011), we can expected that the introduced uncertainties will be rather small.

Finally, we did not take into account the Eddington bias, neither did we consider the details of the source detection and background subtraction algorithms, which will affect to some extent the numbers of detected sources and their $\log N - \log S$ distributions at the faint end. They will also affect the completeness characteristics of the eRASS AGN sample which will have to be accounted for in constructing XLFs. These are usual properties of the flux limited surveys, especially those conducted in the photon counting regime, in the limit of small numbers of counts, where the character of the Poissonian distribution of counts manifests itself strongly. The data analysis methods and techniques to deal with these effects are well known and constitute the standard set of tools in X-ray astronomy. Detailed account for these effects and others (e.g. confusion with extended sources) is beyond the scope of the present paper.

5.4. High Redshift AGN

The density of AGN at high redshifts is of special interest as it can place constraints on the formation scenarios of first supermassive black holes and, hence, on cosmological models (Brandt & Hasinger 2005). Their numbers in the existing surveys including those used to produce the XLF models are very limited. Indeed, the highest redshift bin in the AGN sample of H05 was located at $z = 3.2 - 4.8$ and contained 17 objects. The sample of Miyaji et al. (2000) contained 25 AGN in a somewhat wider redshift interval of $2.3-4.6$ and the sample of Ebrero et al. (2009) had no AGN with $z > 3$. Moreover, these samples are not entirely independent as they were obtained from overlapping sets of deep surveys. There is only a handful of $z > 5$ AGN presently known (Civano et al. 2011, e.g.). Due to low numbers of distant AGN, the XLF at high redshifts is rather poorly constrained. As it is demonstrated below, eRASS will significantly enhance the statistics of high redshift objects.

Our poor knowledge of the AGN XLF at high redshifts limits our ability to accurately predict numbers of high redshift AGN in the eRASS. To estimate the range of uncertainties we calculate their numbers in the soft band using several different XLF models. The resulting cumulative number counts are shown in the Fig. 10. For the purpose of this comparison, the curves were rescaled to reproduce the same number density of AGN as the arithmetic mean of our number density map, introduced in Sect. 3. The correction factors in soft band are 1.33 and 1.32 for H05 with and without redshift cutoff, respectively, 1.15 for Miyaji et al. (2000, Table 3) and 1.88 for Ebrero et al. (2009).

As one can see from the Fig. 10, the number of high redshift objects in the extragalactic sky sample is uncertain by more than an order of magnitude, different predictions ranging for $z > 3$ from $\sim 10^4$ to $\sim 10^5$. For $z > 4$ and $z > 5$ the numbers vary from $\sim 2\,000$ to $\sim 30\,000$ and from ~ 300 to $\sim 9\,000$, respectively. The exponential redshift cutoff of the H05 XLF (cf. solid and dotted black curves) has a significant effect on the numbers of high redshift sources bringing it close to the prediction based on the XLF of Ebrero et al. (2009, red curve). On the other hand, the prediction based on the XLF of H05 without a cutoff (dotted black curve) is close to that of Miyaji et al. (2000, blue curve). This large discrepancy of different XLF at high redshift was already pointed out by Brusa et al. (2011).

For the number of objects in the $z = 3-5$ redshift range our predictions vary from $\sim 8\,000$ to $\sim 90\,000$, the default XLF giving $\sim 30\,000$ objects and without the exponential

[7] `http://www.bo.astro.it/~gilli/counts.html`

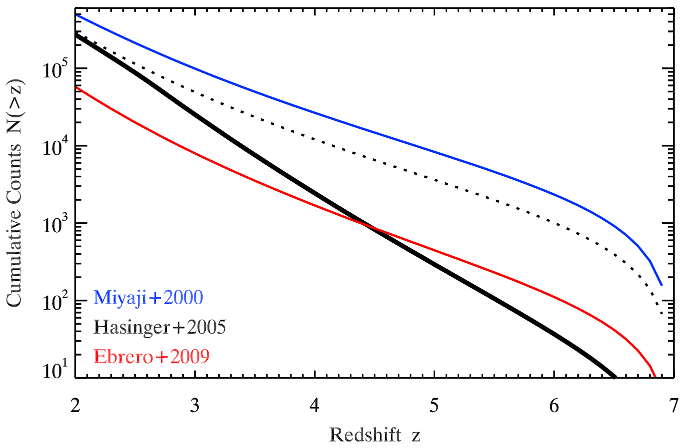

Fig. 10. The numbers of high redshift AGN, $N(>z)$, expected in the soft band for the extragalactic sky after four years. The thick solid black curve shows the prediction based on the default XLF model. Also shown are predictions for the XLF model of Miyaji et al. (2000, Table 3), Hasinger et al. (2005, Table 5, without the exponential redshift cutoff, dotted curve) and Ebrero et al. (2009). To obtain these curves we integrated the XLFs to the maximum redshift of $z = 7$. All curves are rescaled to match the average source density computed with our default model (Sect. 3).

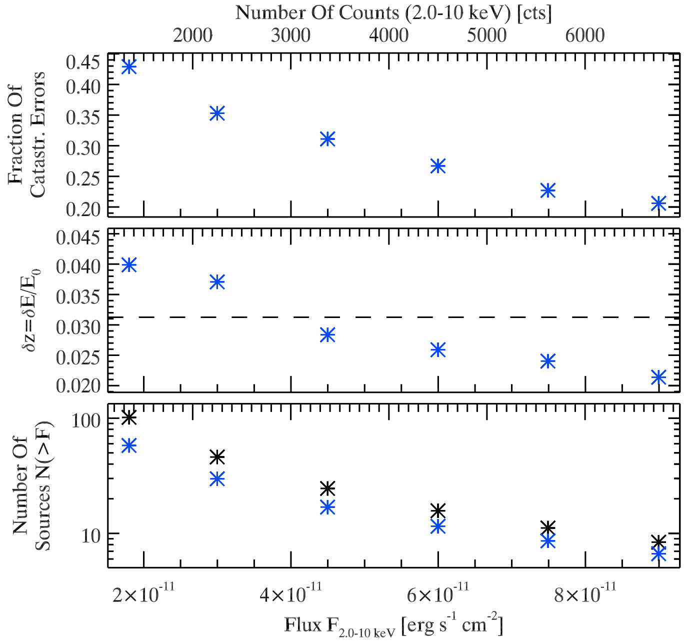

Fig. 11. The feasibility of using the iron $K\alpha$ line for the redshift determination at $z = 0$. See Sect. 6 for details *Top*: Fraction of catastrophic failures. *Middle*: Accuracy of the redshift determination. The black dashed line corresponds to the energy resolution of eROSITA. *Bottom*: Number of sources for which the redshift can be determined with the accuracy shown in the middle panel, the catastrophic failures excluded (black points show only the $\log N - \log S$).

redshift cutoff this number is increased by almost a factor of two.

According to our default hard band XLF, there will be ~ 4 detected AGN in the hard band for the redshift of $z \gtrsim 3.5$. However, the discrepancy between different hard band XLFs is also large, the predictions ranging from ~ 2 (Aird et al. 2010, LADE model of Table 4) up to ~ 200 (La Franca et al. 2005) AGN for $z \gtrsim 3.5$.

The density of high redshift objects will be higher in the ecliptic poles (Fig. 7 and Table 2). For the default soft band XLF, there will be 1 high redshift ($z \gtrsim 5$) AGN every $\sim 5\,\mathrm{deg}^2$, which result in ~ 17 objects in total. Without the exponential redshift cutoff this number is an order of magnitude larger. For the other rescaled XLFs from Fig. 10 the number of objects varies between ~ 20 and ~ 600. Obviously, the higher source density and smaller area will make the search for high redshift objects in the pole regions easier.

6. Redshift determination with the iron Kα line

Presence in the spectra of AGN of the strong Kα line of iron at 6.4 keV opens, in principle, the possibility to determine redshifts by the means of X-ray spectroscopy. Below, we investigate this possibility for the parameters of eRASS characteristics of the eROSITA telescope.

We assume that the continuum spectrum is described by an absorbed power law with he photon index of $\Gamma = 1.9$ and $N_{\mathrm{H}} = 6 \times 10^{20}\ \mathrm{cm}^{-2}$. The shape of the iron Kα line may be rather complex and typicaly includes narrow and broad components (e.g. Gilli et al. 1999; Nandra et al. 2007; Corral et al. 2008; Shu et al. 2010; Chaudhary et al. 2012). However, as the final result of this calculation turns out to be rather negative, we ignore this complexity and use a simple model, consisting of a single Gaussian line at 6.4 keV with the intrinsic width of $\sigma_{\mathrm{Fe}} = 200\,\mathrm{eV}$ and the equivalent width of 150 eV (restframe values).

In order to investigate the detectability of the iron Kα line in the spectra of eRASS AGN, we performed the following simulations. We chose a number of flux values in the $\sim 10^{-11} - 10^{-10}\ \mathrm{erg\,s^{-1}\,cm^{-2}}$ flux range. We fixed the redshift and for each flux value simulated 10^3 spectra using the `phabs(zpowerlw + zgauss)` model in XSPEC (Version 12.7.0, Arnaud 1996). Each spectrum was fit with the same model. In the fit, the parameters σ_{Fe} and N_{H} were fixed, the initial values of other parameters were set at their simulated values. After 10^3 spectra were simulated, the distribution of the best values of the redshift was analyzed. It was fit with a Gaussian distribution, then the points outside $\pm 3\sigma$ range were marked as catastrophic failures, clipped out and the distribution was fit by a Gaussian again. The newly obtained width of the Gaussian determines the accuracy of the redshift determination σ_z. The catastrophic error fraction was then recomputed as a fraction of objects outside $\pm 3\sigma_z$.

Our results for the redshift $z = 0$ are shown in Fig. 11. As one can see from the plot, even at rather large number of counts, $\sim 1\,500$ in the hard band, corresponding to the flux of $\sim 2 \times 10^{-11}\,\mathrm{erg\,s^{-1}\,cm^{-2}}$, the fraction of catastrophic errors is still large, $\sim 40\,\%$. This is caused by the steep decrease of the eROSITA efficiency curve with energy, by more than an order of magnitude between 2 and 6 keV. As a result, even at large total number of counts, the number of counts at ~ 6 keV is too small for reliable line detection in the flux range of interest.

From the middle panel of the Fig.11, the accuracy of the redshift measurements for the remaining $\sim 60\,\%$ of objects may seem to be rather good, $\delta z \lesssim 0.05$. Obviously, it is a result of its definition, which relies on the exclusion of catastrophic failures. Such a definition works well when the latter is small. However, the effect of small δz is nullified when the fraction of catastrophic failures is large. Furthermore, the numbers of objects in this flux range is of the order ~ 100 on the entire extragalactic sky, which is too small to be useful. Majority, if not all of these bright objects will be already known AGN with known redshifts.

The increase of the effective area towards low energies could improve the situation at larger redshifts. For example, for a $z \approx 2$ object, the observed energy of the iron Kα line would fall near the peak of the eROSITA sensitivity and would lower the minimal flux required for reliable redshift determination using the iron Kα line to $\sim 10^{-12}$ erg s^{-1} cm^{-2}. Unfortunately, the relatively small number of $z \sim 2$ objects (a few hundreds) and their low fluxes negate the advantage given by the larger effective area at low energies. However, we note that spectral analysis would still be possible for the sources of known redshift, and that one can still use spectral stacking analysis (e.g. Chaudhary et al. 2010) to study the average properties of the iron Kα line of AGN.

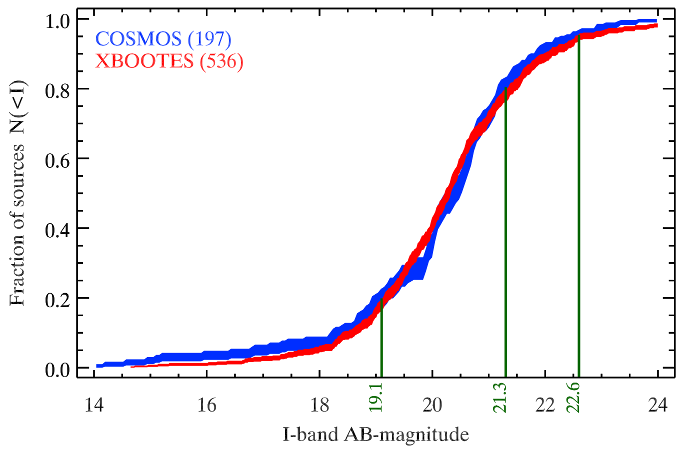

Fig. 12. The cumulative I-band AB-magnitude distribution of AGN in the COSMOS and XBOOTES fields with the $0.5 - 2.0$ keV flux exceeding the four years eRASS detection threshold. The thickness of the curves represents the standard deviation of a binomial distribution. The vertical lines show the photometric sensitivities of the SDSS (21.3 mag) and Pan-STARRS PS1 (22.6 mag) and the magnitude limit for SDSS spectroscopy (19.1 mag).

7. Transient events and flux variability

In the four year survey, eROSITA will scan the whole sky eight times (one full sky survey per half a year). The telescopes rotates around an axis pointing towards the Sun or with some offset (see Sect. 2) and will complete one full circle on the sky every four hours (Predehl et al. 2010). The plane of the scan rotates with the average rate of one degree per day. With this scan geometry, a point on the equator will be scanned every half a year 6 times separated by 4 hours. The number of consecutive scans per one survey increases with latitude as $\propto \cos^{-1}(\delta)$, the poles being scanned continuously every four hours during entire duration of the survey. This scan pattern defines two different sampling rates: $\Delta t_1 = 0.5$ years and $\Delta t_2 = 4$ hours, corresponding to frequencies of $\sim 6 \times 10^{-8}$ and $\sim 7 \times 10^{-5}$ Hz.

For one full sky survey, the average exposure time is ~ 320 sec.[8] At this exposure time, 5 counts corresponds to the flux of $\sim 2 \times 10^{-14}$ and $\sim 4 \times 10^{-13}$ erg s^{-1} cm^{-2} in the soft and hard band respectively. These numbers define the sensitivity of eRASS to the events (e.g. flares) occurring on the ~ 0.5 yr time scale. With eight measurements it is also possible to estimate rms variability on the corresponding timescale. To estimate the sensitivity, we take into account that the sample variance is distributed as $\sigma^2 \chi^2_{\mathcal{N}-1}/(\mathcal{N}-1)$, where σ is the sample rms, $\mathcal{N}$ is the number of points and $\chi^2_{\mathcal{N}-1}$ is the χ^2-distribution with $\mathcal{N}-1$ degrees of freedom. Therefore the 1σ error of the fractional rms^2 determination is $\delta(rms^2) \approx \sqrt{2/(\mathcal{N}-1)} \times (S/N)^{-2}$ where S/N is the signal-to-noise ratio. As an estimate of the sensitivity to source flux variability, we take square root of this expression and obtain $\delta(rms) \approx 0.73 \times (S/N)^{-1}$. Thus, for a $\sim 2 \times 10^{-13}$ erg s^{-1} cm^{-2} soft band source, fractional variability of $rms \sim 20\,\%$ will be detected with a 2σ confidence. On the extragalactic sky, around $\sim 35\,000$ sources are above this flux threshold.

At the average exposure time in a single scan (~ 32 sec), 5 counts correspond to the flux of $\sim 2 \times 10^{-13}$ erg s^{-1} cm^{-2} in the soft band. There is about $\sim 39\,000$ sources on the extragalactic sky above this flux level. This also defines the sensitivity of the eRASS to transient events on the $\sim$hours time scale. Except for the sources in the polar regions, aperiodic variability on these time scales can be measured only for a small number of sources.

[8] For this calculation it is more appropriate to assume an observing efficiency of 100 %.

8. Optical counterparts

To fully explore the potential of the eRASS, extensive optical coverage will be critical. The primary, but not only goal of such a coverage will be to provide the identifications and the redshift information. Detailed discussion of the feasibility and possible strategies of the optical support of the eRASS and its synergies with various on-going and future optical surveys is beyond the scope of this paper, and under extensive discussion in the eROSITA collaboration. In this section we will investigate the expected optical magnitude distribution of the eRASS AGN. To this end, we use results of the XMM-COSMOS (Hasinger et al. 2007) and Bootes (Murray et al. 2005) surveys. For the COSMOS field, we use results of Brusa et al. (2010), who cross-correlated the original XMM-COSMOS catalog of X-ray sources of Cappelluti et al. (2009) with the data of optical survey of the COSMOS field by Capak et al. (2007). From these data we selected sources with the $0.5 - 2.0$ keV flux exceeding the eRASS 4-years detection threshold, $S_{0.5-2.0\,\mathrm{keV}} \geq 10^{-14}$ erg s^{-1} cm^{-2}, being not brighter than $I = 14.0$ mag and of high identification reliability. This selection resulted in a sample of 204 sources for which we obtained I-band AB-magnitude distribution.

We made similar analysis for the XBootes field, cross-correlating the X-ray and optical catalogs for this field (Kenter et al. 2005; Brand et al. 2006). We selected point-like sources (class $\geq$ 0.50) with $S_{0.5-2.0\,\mathrm{keV}} \geq 10^{-14}\,\mathrm{erg\,s^{-1}\,cm^{-2}}$, for which optical counterpart was found (St = 1) with high probability of true identification (Popt $\geq$ 0.95). We thus selected 540 X-ray sources, for which we computed the cumulative I-band magnitude distribution, converting the Vega magnitudes to AB-magnitudes with the conversion factor from Blanton & Roweis (2007, Table 1): $\mathrm{m_{AB}} = \mathrm{m_{Vega}} + \mathrm{m_{AB}(Vega)}$ with $\mathrm{m_{AB}(Vega)} = 0.45$ for the I-band.

The so obtained I-band magnitude distributions for the COSMOS and Bootes fields are plotted in the Fig.12. They show good agreement between results for two different fields, meaning that we have a very good knowledge of the expected magnitude distribution of sources at the bright X-ray fluxes. Comparing this distribution with the limiting magnitude of the Sloan Digital Sky Survey in the i-band, 21.3 mag at the 95 % completeness (Abazajian et al. 2009), we conclude that about ≈ 80 % of the eRASS AGN in the SDSS sky will have optical counterparts. Taking into account the sky area covered by SDSS, $\sim 14\,500\,\mathrm{deg}^2$, we estimate, that about ∼ 1/3 of eRASS objects will have an optical counterpart in the SDSS photometric catalog. About ≈ 20 % of objects will be brighter than the spectroscopic limit of the SDSS, $i = 19.1$ mag for Quasars at $z < 3$ (Richards et al. 2002), i.e. some fraction of these objects will have SDSS spectra.

Doing the same analyze with the half a year sensitivity of eRASS, we expecte that almost all eRASS AGN in the SDSS sky will have optical counterparts.

One can see from Fig. 12, that 95 % of eRASS AGN will be brighter than $I \approx 22.5$ mag ($R \approx 23.0$ mag). The Pan-STARRS PS1 3π survey will exceed this depth with its expected sensitivity of ≈ 22.6 mag in one visit (Chambers & the Pan-STARRS Team 2006). The 3 years PS1 sensitivity in the I-band will reach ≈ 23.9 mag and will cover virtually all eRASS objects in the field of the 3π survey .

9. Summary and conclusions

In this paper, we computed various statistical characteristics of the expected eRASS AGN sample, including their luminosity and redshift distributions and magnitude distributions of their optical counterparts.

The eROSITA all-sky survey will produce an unprecedented sample of about 3 million X-ray selected AGN. With the median redshift of $z \approx 1$, about ≈ 40 % of eRASS objects will be located between redshifts $z = 1$ and $z = 2$ (Fig.7). We predict that about $\sim 10^4 - 10^5$ AGN beyond redshift $z = 3$ and about $\sim 2\,000 - 30\,000$ AGN beyond the redshift $z = 4$, the exact numbers depending on the behavior of the AGN XLF in the high redshift and luminosity regimes (Fig.9). The eRASS AGN sample will open the possibility to study the growth of the supermassive black holes and their relation to the large scale structure to unprecedented detail. Potentially, it will also help to constrain cosmological parameters. Importantly, it will permit to conduct these studies beyond redshift $z = 1$, rather poorly covered by the modern optical surveys.

To fully exploit the potential of eRASS, an extensive optical support will be critical. One of the main goals of optical follow-up will be to provide redshifts for eRASS AGN, but its importance will reach far beyond this, including, for example, studies of the co-evolution of supermassive black holes and their host galaxies. With the capabilities of the currently available facilities and their time allocation strategies, the measurement of optical spectra for the entire sample of the ∼ 3 million objects does not appear to be achievable on realistic time scales. However upcoming hardware and survey programs and proposal (e.g. 4MOST, de Jong et al. 2012) can make this task more realistic, especially for some limited areas of sky. Furthermore, introduction of the mutli-band photometry and further improvements of the photometric redshift measurement techniques will make determination of photometric redshifts for large sample of eRASS AGN possible (Salvato et al. 2011; Saglia et al. 2012).

To further illustrate the potential of the eRASS sample in the limited sky areas, we show in the Fig. 13 the number of objects per redshift bin as a function of redshift, for several luminosity groups. For this calculation we chose a sky area of $14\,000\,\mathrm{deg}^2$, similar to the area of the Sloan Digital Sky Survey and considered rather broad redshift bins, consistent with the expected accuracy of photometric redshifts based on the multi-band photometry Salvato et al. (2011). It is obvious from the Fig. 13, that even rather coarse redshift information over relatively limited areas of sky is capable to deliver unprecedented samples of AGN.

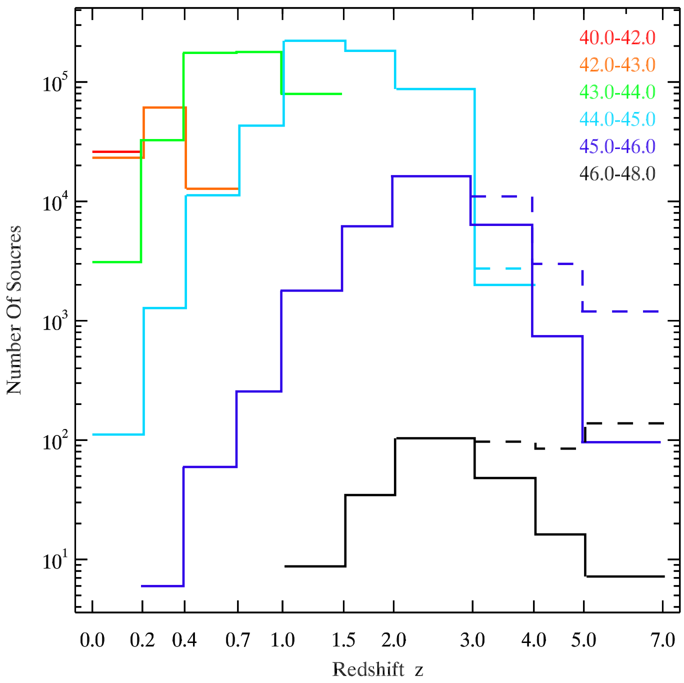

Fig. 13. The number of eRASS AGN as a function of the redshift for different luminosity groups in the sky area, similar to that covered by SDSS ($14\,000\,\mathrm{deg}^2$). The dashed histograms show predictions based on the XLF without exponential high-redshift cut-off (Sect. 4).

Acknowledgements. A. Kolodzig acknowledges support from and participation in the International Max-Planck Research School (IMPRS) on Astrophysics at the Ludwig-Maximilians University of Munich (LMU). We thank Jan Robrade for the exposure time map of eROSITA and additional calculations, Peter Friedrich for the details about the PSF of eROSITA, Thomas Boller for the details about the eROSITA background calculation, Andrea Merloni for useful discussions and Peter Predehl for background information about eROSITA.

References

Abazajian, K. N., Adelman-McCarthy, J. K., Agüeros, M. A., et al. 2009, ApJS, 182, 543

Aird, J., Nandra, K., Laird, E. S., et al. 2010, MNRAS, 401, 2531

Anders, E. & Grevesse, N. 1989, Geochim. Cosmochim. Acta, 53, 197

Arnaud, K. A. 1996, in Astronomical Society of the Pacific Conference Series, Vol. 101, Astronomical Data Analysis Software and Systems V, ed. G. H. Jacoby & J. Barnes, 17

Blanton, M. R. & Roweis, S. 2007, AJ, 133, 734

Brand, K., Brown, M. J. I., Dey, A., et al. 2006, ApJ, 641, 140

Brandt, W. N. & Hasinger, G. 2005, ARA&A, 43, 827

Brusa, M., Civano, F., Comastri, A., et al. 2010, ApJ, 716, 348

Brusa, M., Comastri, A., Gilli, R., et al. 2009, ApJ, 693, 8

Brusa, M., Gilli, R., Civano, F., et al. 2011, Memorie della Societa Astronomica Italiana Supplementi, 17, 106

Burlon, D., Ajello, M., Greiner, J., et al. 2011, ApJ, 728, 58

Capak, P., Aussel, H., Ajiki, M., et al. 2007, ApJS, 172, 99

Cappelluti, N., Brusa, M., Hasinger, G., et al. 2009, A&A, 497, 635

Chambers, K. & the Pan-STARRS Team. 2006, in The Advanced Maui Optical and Space Surveillance Technologies Conference

Chaudhary, P., Brusa, M., Hasinger, G., Merloni, A., & Comastri, A. 2010, A&A, 518, A58

Chaudhary, P., Brusa, M., Hasinger, G., et al. 2012, A&A, 537, A6

Civano, F., Brusa, M., Comastri, A., et al. 2011, ArXiv e-prints

Corral, A., Page, M. J., Carrera, F. J., et al. 2008, A&A, 492, 71

de Jong, R. S., Bellido-Tirado, O., Chiappini, C., et al. 2012, ArXiv e-prints

Ebrero, J., Carrera, F. J., Page, M. J., et al. 2009, A&A, 493, 55

Georgakakis, A., Nandra, K., Laird, E. S., Aird, J., & Trichas, M. 2008, MNRAS, 388, 1205

Gilli, R., Comastri, A., Brunetti, G., & Setti, G. 1999, New A, 4, 45

Hasinger, G., Cappelluti, N., Brunner, H., et al. 2007, ApJS, 172, 29

Hasinger, G., Miyaji, T., & Schmidt, M. 2005, A&A, 441, 417

Hiroi, K., Ueda, Y., Akiyama, M., & Watson, M. G. 2012, ApJ, 758, 49

Hogg, D. W. 1999, ArXiv Astrophysics e-prints

Kalberla, P. M. W., Burton, W. B., Hartmann, D., et al. 2005, A&A, 440, 775

Kenter, A., Murray, S. S., Forman, W. R., et al. 2005, ApJS, 161, 9

Kim, M., Wilkes, B. J., Kim, D.-W., et al. 2007, ApJ, 659, 29

Komatsu, E., Smith, K. M., Dunkley, J., et al. 2011, ApJS, 192, 18

La Franca, F., Fiore, F., Comastri, A., et al. 2005, ApJ, 635, 864

Lumb, D. H., Warwick, R. S., Page, M., & De Luca, A. 2002, A&A, 389, 93

Merloni, A., Predehl, P., Becker, W., et al. 2012, ArXiv e-prints

Miyaji, T., Hasinger, G., & Schmidt, M. 2000, A&A, 353, 25

Moretti, A., Campana, S., Lazzati, D., & Tagliaferri, G. 2003, ApJ, 588, 696

Murray, S. S., Kenter, A., Forman, W. R., et al. 2005, ApJS, 161, 1

Nandra, K., O'Neill, P. M., George, I. M., & Reeves, J. N. 2007, MNRAS, 382, 194

Perinati, E., Tenzer, C., Santangelo, A., et al. 2012, Experimental Astronomy, 33, 39

Predehl, P., Andritschke, R., Böhringer, H., et al. 2010, in Society of Photo-Optical Instrumentation Engineers (SPIE) Conference Series, Vol. 7732, Society of Photo-Optical Instrumentation Engineers (SPIE) Conference Series

Prokopenko, I. G. & Gilfanov, M. R. 2009, Astronomy Letters, 35, 294

Richards, G. T., Fan, X., Newberg, H. J., et al. 2002, AJ, 123, 2945

Saglia, R. P., Tonry, J. L., Bender, R., et al. 2012, ApJ, 746, 128

Salvato, M., Ilbert, O., Hasinger, G., et al. 2011, ApJ, 742, 61

Shu, X. W., Yaqoob, T., & Wang, J. X. 2010, ApJS, 187, 581

Silverman, J. D., Green, P. J., Barkhouse, W. A., et al. 2008, ApJ, 679, 118

Tenzer, C., Warth, G., Kendziorra, E., & Santangelo, A. 2010, in Society of Photo-Optical Instrumentation Engineers (SPIE) Conference Series, Vol. 7742, Society of Photo-Optical Instrumentation Engineers (SPIE) Conference Series

Truemper, J. 1993, Science, 260, 1769

Ueda, Y., Akiyama, M., Ohta, K., & Miyaji, T. 2003, ApJ, 598, 886

Voges, W., Aschenbach, B., Boller, T., et al. 1999, VizieR Online Data Catalog, 9010, 0